The Astrophysical Journal Letters, 900:L36 (11pp), 2020 September 10 https://doi.org/10.3847/2041-8213/abb19c

Electron Heating in Perpendicular Low-beta Shocks

Aaron Tran and Lorenzo Sironi
Department of Astronomy, Columbia University, 550 W 120th Street, MC 5246, New York, NY 10027, USA; aaron.tran@columbia.edu
Received 2020 May 20; revised 2020 August 18; accepted 2020 August 19; published 2020 September 10

Abstract

Collisionless shocks heat electrons in the solar wind, interstellar blast waves, and hot gas permeating galaxy clusters. How much shock heating goes to electrons instead of ions, and what plasma physics controls electron heating? We simulate 2D perpendicular shocks with a fully kinetic particle-in-cell code. For magnetosonic Mach number $\mathcal{M}_{\rm ms} \sim 1$–10 and plasma beta $\beta_{\rm p} \lesssim 4$, the post-shock electron/ion temperature ratio $T_{\rm e}/T_{\rm i}$ decreases from 1 to 0.1 with increasing $\mathcal{M}_{\rm ms}$. In a representative $\mathcal{M}_{\rm ms} = 3.1$, $\beta_{\rm p} = 0.25$ shock, electrons heat above adiabatic compression in two steps: ion-scale $E_\parallel = \boldsymbol{E} \cdot \hat{\boldsymbol{b}}$ accelerates electrons into streams along $\boldsymbol{B}$, which then relax via two-stream-like instability. The $\boldsymbol{B}$-parallel heating is mostly induced by waves; $\boldsymbol{B}$-perpendicular heating is mostly adiabatic compression by quasi-static fields.

Unified Astronomy Thesaurus concepts: Shocks (2086); Planetary bow shocks (1246); Space plasmas (1544); Plasma astrophysics (1261)

Supporting material: animations, figure sets, machine-readable table

1. Introduction

Electron heating in collisionless shocks—stated as post-shock electron/ion temperature ratio $T_{\rm e}/T_{\rm i}$—is not constrained by magnetohydrodynamic (MHD) shock jump conditions. How much do electrons heat, and how do they heat? A prediction for $T_{\rm e}/T_{\rm i}$ can constrain models for gas accretion onto galaxy clusters (Avestruz et al. 2015) and cosmic-ray acceleration in supernova remnants (Helder et al. 2010; Yamaguchi et al. 2014; Hovey et al. 2018). Detailed study of the electron heating physics can also help us interpret new high-resolution data from the Magnetospheric Multiscale Mission (Chen et al. 2018; Goodrich et al. 2018; Cohen et al. 2019).

In the heliosphere, shocks of magnetosonic Mach number $\mathcal{M}_{\rm ms} \gtrsim 2$–3 heat electrons beyond adiabatic compression via a two-step process: electrons accelerate in bulk along $\boldsymbol{B}$ toward the shock downstream, then relax into "flat-top" distributions in $\boldsymbol{B}$-parallel velocity (Feldman et al. 1982, 1983; Chen et al. 2018). Two mechanisms—quasi-static direct current (DC) fields and plasma waves—may drive $\boldsymbol{B}$-parallel acceleration. In the DC mechanism, an electric potential jump in the shock layer (i.e., a quasi-static electric field that points along shock normal) accelerates electrons in bulk (Feldman et al. 1983; Goodrich & Scudder 1984; Scudder et al. 1986; Scudder 1996; Hull et al. 2001; Lefebvre et al. 2007; Schwartz 2014). The DC electron energy gain scales with $\cos^2\theta$, where θ is the angle between $\boldsymbol{B}$ and shock normal (Goodrich & Scudder 1984). We expect no heating in exactly planar perpendicular shocks, but shock rippling from ion-scale waves (Lowe & Burgess 2003; Johlander et al. 2016; Hanson et al. 2019) can bend $\boldsymbol{B}$, alter θ, and enable DC heating. Plasma waves with nonzero $E_\parallel = \boldsymbol{E} \cdot \hat{\boldsymbol{b}}$, such as oblique whistlers, can also provide electron bulk acceleration and thus heating (Wilson et al. 2014a, 2014b). Such plasma waves are intrinsic to shock structure (Krasnoselskikh et al. 2002; Wilson et al. 2009, 2012; Dimmock et al. 2019) and may be sustained by free energy from, e.g., shock-reflected ions (Wu et al. 1984; Matsukiyo & Scholer 2006; Muschietti & Lembège 2017).

In this Letter, we study thermal electron heating in multi-dimensional particle-in-cell (PIC) simulations of perpendicular shocks with realistic structure (requiring high ion/electron mass ratio $m_{\rm i}/m_{\rm e}$; Krauss-Varban et al. 1995; Umeda et al. 2012a, 2014) and high grid resolution to resolve electron scattering and relaxation after $\boldsymbol{B}$-parallel bulk acceleration.

2. Method

We simulate collisionless 2D (x–y) ion–electron shocks using the relativistic PIC code TRISTAN-MP (Buneman 1993; Spitkovsky 2005). We inject plasma with velocity $-u_0\hat{\boldsymbol{x}}$ and magnetic field $B_0\hat{\boldsymbol{y}}$ from the simulation domain's right-side (upstream) boundary. Injected plasma reflects from a conducting wall at $x = 0$, forming a shock that travels toward $+\hat{\boldsymbol{x}}$. The shocked downstream plasma has zero bulk velocity, and the upstream $\boldsymbol{B}$ is perpendicular to the shock normal, so $\theta = 90°$. The simulation domain expands along $+\hat{\boldsymbol{x}}$ to keep the right-side boundary $\gtrsim 1.5\, r_{\rm Li}$ ahead of the shock front (Sironi & Spitkovsky 2009, Section 2), where $r_{\rm Li} = u_0/\Omega_{\rm i}$ is a characteristic ion Larmor radius; we checked that shock heating physics is not artificially affected by the right-side boundary. Upstream ions and electrons have equal density n_0 and temperature T_0. The plasma frequencies $\omega_{\rm p\{i,e\}} = \sqrt{4\pi n_0 e^2/m_{\rm \{i,e\}}}$ and cyclotron frequencies $\Omega_{\rm \{i,e\}} = eB_0/(m_{\rm \{i,e\}}c)$, where subscripts i and e denote ions and electrons. We use Gaussian CGS units throughout.

Our fiducial simulations have ion/electron mass ratio $m_{\rm i}/m_{\rm e} = 625$ and total plasma beta $\beta_{\rm p} = 16\pi n_0 k_{\rm B} T_0/{B_0}^2 = 0.25$. The fast magnetosonic, sonic, and Alfvén Mach numbers are $\mathcal{M}_{\rm ms} = u_{\rm sh}/\sqrt{{c_{\rm s}}^2 + {v_{\rm A}}^2} = 1$–10, $\mathcal{M}_{\rm s} = u_{\rm sh}/c_{\rm s} = 3$–20, and $\mathcal{M}_{\rm A} = u_{\rm sh}/v_{\rm A} = 1.5$–10. The sound speed $c_{\rm s} = \sqrt{2\Gamma k_{\rm B} T_0/(m_{\rm i} + m_{\rm e})}$, Alfvén speed $v_{\rm A} = B_0/\sqrt{4\pi n_0(m_{\rm i} + m_{\rm e})}$, and $u_{\rm sh}$ is the speed of upstream plasma in the shock's rest frame; for nonrelativistic speeds, $u_{\rm sh} = u_0/(1 - 1/r)$, where $r \leqslant 4$ is the MHD shock-compression ratio. The one-fluid adiabatic index Γ is not known a priori, but it is set self-consistently by the degree of ion and electron isotropization. We report Mach numbers assuming $\Gamma = 2$, which overestimates $\mathcal{M}_{\rm ms}$ by $\sim$1–10% for stronger shocks that isotropize ions/electrons and have $\Gamma \approx 5/3$.

The grid cell size $\Delta x = \Delta y = 0.1c/\omega_{\rm pe}$ and the time step $\Delta t = 0.045\omega_{\rm pe}^{-1}$ so that $c = 0.45\Delta x/\Delta t$. Upstream plasma has 16 particles per cell per species. We smooth the electric current with 32 sweeps of a three-point binomial ("1–2–1") filter at each time step (Birdsall & Langdon 1991, Appendix C). The $N = 32$ sweeps approximate a Gaussian filter with standard deviation $\sqrt{N/2} = 4$ cells or $0.4c/\omega_{\rm pe}$. The filter's half-power cutoff is at wavenumber $k \approx \sqrt{2/N}(\Delta x)^{-1} = 2.5(c/\omega_{\rm pe})^{-1}$, which implies 50% damping at wavelength $\lambda \approx \pi\sqrt{2N}\Delta {\rm x} = 2.5(c/\omega_{\rm pe})$. Electron-scale waves may be damped, but we will later show that electron-scale waves mainly scatter rather than heat. We simulated 2D $\mathcal{M}_{\rm ms} = 3.1$, $\beta_{\rm p} = 0.25$ shocks with 4$\times$ larger or smaller sweep number N; the ratio $T_{\rm e}/T_{\rm i}$ did not change much. We adjust T_0, u_0, and B_0 to control $\mathcal{M}_{\rm ms}$ and $\beta_{\rm p}$ while keeping shocked electrons nonrelativistic, i.e., post-shock $k_{\rm B}T_{\rm e} \lesssim 0.05 m_{\rm e}c^2$. The ratio $\tau = \omega_{\rm pe}/\Omega_{\rm e} = 2.5$–11 ($\tau \gg 1$ for solar wind and astrophysical settings). The transverse (y) width is 2.9–5.8 $c/\omega_{\rm pi}$ = 720–1440 cells. Simulation durations are 10–20 $\Omega_{\rm i}^{-1}$ = 932–2736 $\omega_{\rm pi}^{-1}$ so that post-shock $T_{\rm e}/T_{\rm i}$ reaches steady state. The temperatures $T_{\{\rm i,e\}}$, $T_{\{\rm i,e\}\parallel}$, and $T_{\{\rm i,e\}\perp}$ are moments of the particle distribution in a 5^N cell region, where $N \in \{1, 2, 3\}$ is the domain dimensionality. The comoving frame boost for moment calculation uses a fluid velocity also averaged over 5^N cells. All $\parallel$- and $\perp$-subscripted quantities are taken with respect to local $\boldsymbol{B}$.

Figure 1 shows a representative simulation. Ions transmit or reflect at the shock ramp (Figures 1(a)–(b)). The shock front is rippled (Figure 1(c)). A net E_x potential exists across the shock, and E_x is also modulated by the $\boldsymbol{B}$ rippling wavelength (Figures 1(b)–(c)). Reflected ions accelerate in the motional field $E_z = u_0B_0/c$ before reentering the shock (Leroy et al. 1982); this lowers $T_{\rm e}/T_{\rm i}$ in the shock foot (Figure 1(d)). Electrons heat above adiabatic expectation in the shock ramp and settle to $T_{\rm e}/T_{\rm i} \approx 0.4$; no appreciable heating occurs after the shock ramp (Figure 1(d)). The fluid adiabatic prediction in Figure 1(d) is $T_{\rm e,ad}/(T_{\rm i} + T_{\rm e} - T_{\rm e,ad})$, using measured $T_{\rm i}$ and $T_{\rm e}$ and assuming $T_{\rm e,ad} = T_0[1 + 2(n/n_0)^{\Gamma-1}]/3$ with $\Gamma = 2$.

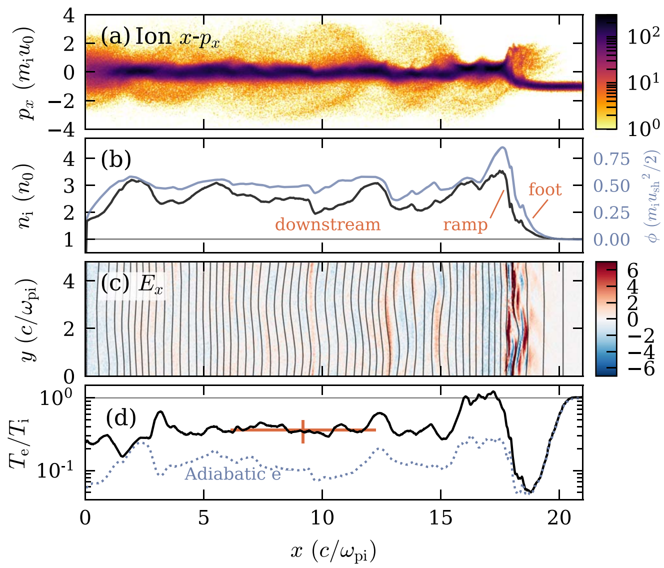

Figure 1. Overview of $\mathcal{M}_{\rm ms} = 3.1$, $\beta_{\rm p} = 0.25$ shock at $t = 1253\,\omega_{\rm pi}^{-1} = 14.2\,\Omega_{\rm i}^{-1}$. (a) Ion x–p_x phase-space distribution for full domain, where p_x is ion x-momentum normalized to upstream momentum $m_{\rm i}u_0$. (b) Ion density $n_{\rm i}/n_0$ (black) and electromotive force $\phi(x) = -\int_{\infty}^{x} E_x(x')dx'$ in units of $m_{\rm i}u_{\rm sh}{}^2/2$ (light blue). Both curves are 1D volume-weighted averages over y. The shock foot, ramp, and downstream are annotated. (c) Electric field E_x normalized to upstream motional field u_0B_0/c with magnetic field lines overlaid. $\boldsymbol{B}$ points up, i.e., along $+\hat{\boldsymbol{y}}$. (d) $T_{\rm e}/T_{\rm i}$, density-weighted y average (black), compared to prediction for fluid adiabatic electron heating defined in the text (blue dotted). Orange cross is the starred measurement in Figure 2(a); cross width is the measurement region, and cross height is the standard deviation over 2D region delimited by cross width. An animation of this figure shows time evolution from $t = 0$ to $1253\,\omega_{\rm pi}^{-1}$ and demonstrates that the temperature ratio $T_{\rm e}/T_{\rm i}$ stabilizes $\sim$3 $c/\omega_{\rm pi}$ downstream of the shock ramp. The realtime duration of the video is 4 s.

(An animation of this figure is available.)

3. Shock Parameter Scaling

We measure post-shock $T_{\rm e}/T_{\rm i}$ (Figure 1(c)) as a function of $\mathcal{M}_{\rm ms}$ for many simulations with varying dimensionality, magnetic field orientation θ, $m_{\rm i}/m_{\rm e}$, and $\beta_{\rm p}$. We also adjust domain width, particle resolution, and current smoothing to control noise and computing cost. In simulations with $\theta < 90°$, the right-side boundary expands at $\max(u_{\rm sh}, 0.5c\cos\theta)$ to retain shock-reflected electrons streaming along $\boldsymbol{B}$.

We show the post-shock $T_{\rm e}/T_{\rm i}$ for our fiducial 2D $m_{\rm i}/m_{\rm e} = 625$ shocks with in-plane upstream magnetic field $B_0\hat{\boldsymbol{y}}$ in Figure 2(a). These fiducial simulations are converged in $T_{\rm e}/T_{\rm i}$ with respect to transverse (y) width. For perpendicular shocks, we find that electron heating beyond adiabatic compression requires 2D geometry with in-plane $\boldsymbol{B}$. Corresponding 2D simulations with out-of-plane $\boldsymbol{B}$ (along $\hat{z}$) and 1D simulations heat electrons by compression alone (Figure 2(a)). At $\mathcal{M}_{\rm ms} \sim 5$–10, the 2D simulations with out-of-plane $\boldsymbol{B}$ and 1D simulations show weak super-adiabatic heating in the shock layer, but the $T_{\rm e}/T_{\rm i}$ measurement is also less precise due to numerical heating. Shimada & Hoshino (2000, 2005) saw strong electron heating in 1D perpendicular $m_{\rm i}/m_{\rm e} = 20$ shocks due to Buneman instability between shock-reflected ions and incoming electrons. The higher $m_{\rm i}/m_{\rm e} = 625$ suppresses the Buneman instability in our 1D shocks.

Can DC heating in a 2D rippled shock—i.e., varying local magnetic field angle due to self-generated waves—explain the super-adiabatic electron heating seen in our fiducial 2D simulations? To estimate the DC heating from varying θ, we perform 1D oblique shock simulations with varying $\theta < 90°$ (Figure 2(b)); recall that θ is the angle between $\boldsymbol{B}$ and shock normal. The 1D setup keeps quasi-static shock structure (averaged over shock reformation cycles) and should retain DC heating while excluding waves oblique to the shock normal. We do find super-adiabatic heating in 1D oblique shocks. Electrons heat more for lower θ, which is qualitatively consistent with DC field heating (Goodrich & Scudder 1984). For our representative $\mathcal{M}_{\rm ms} = 3.1$ shock, which has local ripple $\theta \gtrsim 80°$ (Figure 4(f)), the DC heating inferred from 1D oblique shock simulations appears too low to explain the full amount of super-adiabatic heating (Figure 2(b), box).

Our fiducial 2D perpendicular shocks appear converged in mass ratio at $m_{\rm i}/m_{\rm e} \sim 200-625$ (Figure 2(c)), consistent with prior simulations (Umeda et al. 2012a, 2014) and theory (Krauss-Varban et al. 1995). For $m_{\rm i}/m_{\rm e} = 20$–625, 2D shocks agree on $T_{\rm e}/T_{\rm i}$ to within a factor of 2–3. A set of 3D $m_{\rm i}/m_{\rm e} = 49$ simulations with narrower transverse width, 2.7$c/\omega_{\rm pi}$, shows good agreement too. Agreement between 2D and 3D for $m_{\rm i}/m_{\rm e} = 49$ suggests that 2D simulations with in-plane $\boldsymbol{B}$ include the essential physics for electron heating.

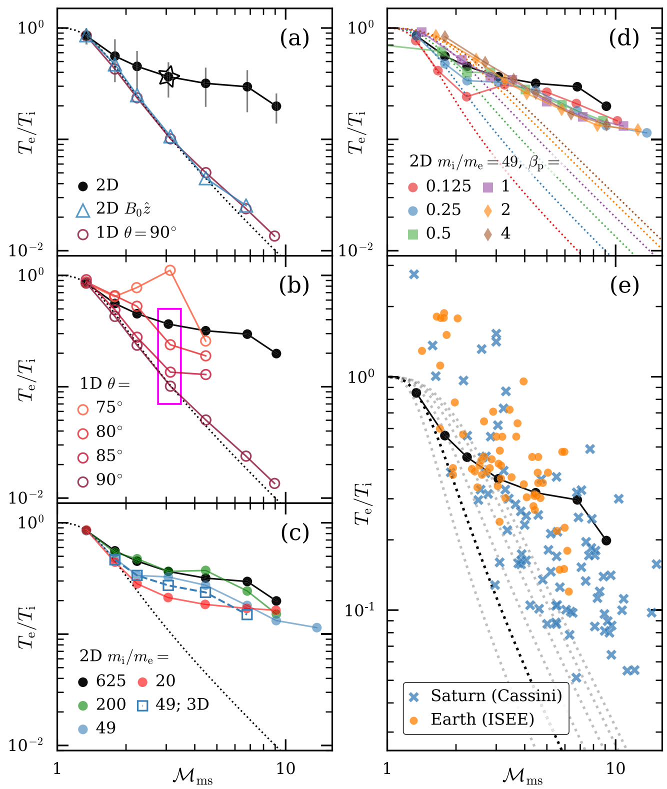

Figure 2. Post-shock T_e/T_i dependence on $\mathcal{M}_{ms}$ for various setups. All panels: black curve is T_e/T_i from fiducial 2D $m_i/m_e = 625$, $\beta_p = 0.25$ shocks. Dotted curves are expected T_e/T_i from MHD shock jump conditions, assuming adiabatic electron heating alone. (a) Varying geometry. 2D domain with out-of-plane $B_0\hat{z}$ (triangles) and 1D domain (hollow circles). Starred datum appears in Figures 1 and 3–4. Error bars on the black curve are the standard deviation of T_e/T_i within the measurement region. (b) 1D domain, varying θ. Darkest hollow circles ($\theta = 90°$) same as (a). (c) 2D domain, varying m_i/m_e. Dashed cyan curve with square markers comprises 3D $m_i/m_e = 49$ simulations. (d) 2D domain, $m_i/m_e = 49$, varying β_p. Dotted curves are the adiabatic expectation as in panels (a)–(c), with β_p increasing from left to right. (e) Comparison to solar wind bow shock measurements at Earth (orange circles; Schwartz et al. 1988) and Saturn (blue crosses; Masters et al. 2011) as compiled by Ghavamian et al. (2013). Five Saturn measurements with $\mathcal{M}_{ms} > 20$ are not shown.

To see how heating depends on β_p, we reduce m_i/m_e to 49 and sweep β_p over 0.125–4 (Figure 2(d)). Electron heating increases above adiabatic at $\mathcal{M}_{ms} \sim 2$–3 for all β_p. At $\mathcal{M}_{ms} \sim 3$–5 and $\beta_p \leqslant 1$, two-step $\boldsymbol{B}$-parallel electron heating (which we describe below) operates for all $\beta_p \lesssim 1$. At $\mathcal{M}_{ms} \sim 3$–5 and $\beta_p \gtrsim 2$, a distinct electron cyclotron whistler instability is expected to heat electrons instead (Guo et al. 2017, 2018). At $\mathcal{M}_{ms} \gtrsim 5$, shock structure is more complex, which we do not explore here. The relationship between T_e/T_i and $\mathcal{M}_{ms}$ does not appear to depend on β_p for $\mathcal{M}_{ms} \gtrsim 4$.

Our fiducial $T_e/T_i - \mathcal{M}_{ms}$ data are order-of-magnitude consistent with measurements from solar wind bow shocks (Figure 2(e)), replotted from Ghavamian et al. (2013). The Saturn data are uncertain in both T_e/T_i and $\mathcal{M}_{ms}$ due to a lack of ion temperature measurements from Cassini (Masters et al. 2011), so $\mathcal{M}_{ms} = 0.671\mathcal{M}_A$ (equivalent to $\beta_p \sim 1.5$) is assumed following Ghavamian et al. (2013); we note $\beta_p \sim 1.5$ is a typical value (Richardson 2002). The Earth data have $\beta_p \sim 0.1$–1 and use directly measured ion and electron temperatures from the ISEE spacecraft (Schwartz et al. 1988).

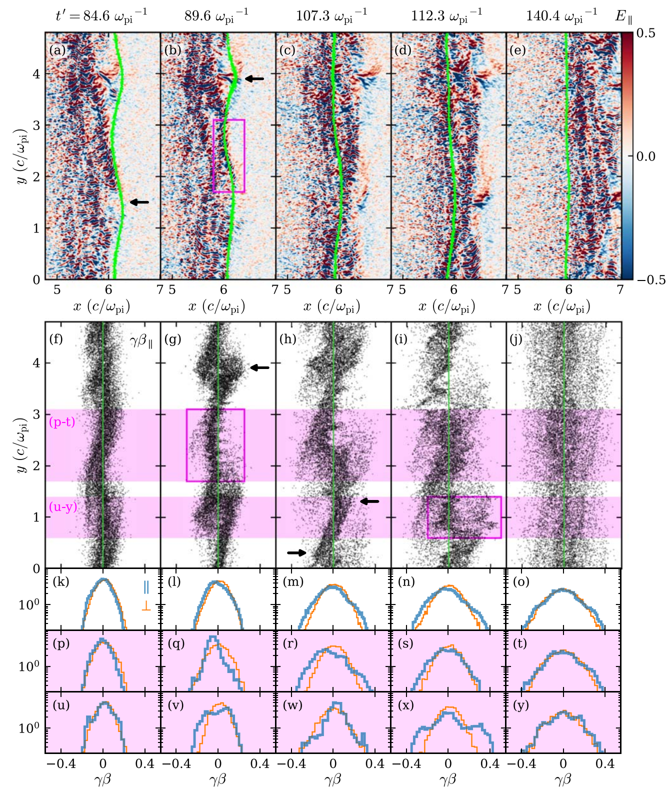

Figure 3. Phase spacetime evolution (left to right) of the electron sample in $\mathcal{M}_{ms} = 3.1$, $\beta_p = 0.25$ shock. (a)–(e) $E_\parallel$ normalized to upstream motional field u_0B_0/c with the electron sample overlaid (green dots). Colormap saturates on small-scale waves. (f)–(j) $\gamma\beta_\parallel$–y phase space of the electron sample. Green vertical lines mark $\gamma\beta_\parallel = 0$. (k)–(o) 1D $\gamma\beta_{\{\parallel,\perp\}}$ distribution of the full electron sample. Thick blue curve is $\gamma\beta_\parallel$; orange curve is $\gamma\beta_\perp$. (p)–(t) Similar to (k)–(o), but only electrons within $y = 1.7$–$3.1\ c/\omega_{pi}$. (u)–(y) Similar to (k)–(o), but only electrons within $y = 0.6$–$1.4\ c/\omega_{pi}$. Here $\gamma = 1/\sqrt{1-\beta^2}$ and $\beta_{\{\parallel,\perp\}} = v_{\{\parallel,\perp\}}/c$. Arrows and boxes discussed in the text.

Both data sets are mostly quasi-perpendicular, with a majority of shocks having $50° < \theta < 90°$ (Schwartz et al. 1988; Masters et al. 2011).

4. Electron Heating Physics

For further study, we choose the weakest 2D $m_i/m_e = 625$, $\beta_p = 0.25$ shock with significant super-adiabatic heating: our representative $\mathcal{M}_{ms} = 3.1$ simulation (Figures 1 and 2(a)). We redo this simulation with higher resolution: $\Delta x = \Delta y = 0.05\ c/\omega_{pe}$ (keeping $c = 0.45\Delta x/\Delta t$), 64 particles per cell per species, and 64 current filter passes per time step. The current filter approximates a Gaussian with standard deviation ~5.7 cells or $0.28c/\omega_{pe}$; the filter's half-power cutoff is at wavenumber $k \approx 3.5(c/\omega_{pe})^{-1}$, which means 50% damping at wavelength $\lambda \approx 1.8c/\omega_{pe}$. We then select 15,898 electron particles between $x = 8.00$–$8.02c/\omega_{pi}$ at $t' \equiv t - 324\ \omega_{pi}^{-1} = 0$, located $4\ c/\omega_{pi} = 2\ r_{Li}$ ahead of the shock ramp, and monitor their phase-space evolution (Figure 3) and energy gain (Figure 4) through the shock. The perpendicular upstream $\boldsymbol{B}$ confines particles within a narrow magnetic flux tube and prevents particle drift from downstream to upstream.

Elongated, ion-scale $E_\parallel$ waves accelerate electrons along $\boldsymbol{B}$ in the shock foot and ramp. These waves have

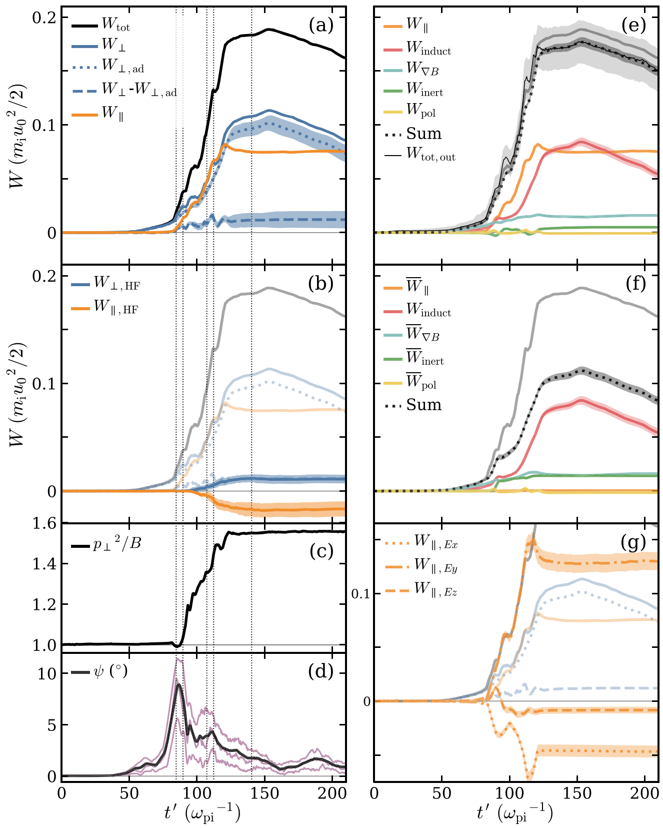

Figure 4. Mean work done on the electron sample over time, normalized to upstream ion drift kinetic energy. Vertical dotted lines are snapshot times in Figure 3. Faded curves in (b), (e), (f), and (g) same as (a). Shaded regions are estimated error on coarse-time-step integrated quantities. (a) Decomposition into $W_\parallel$, $W_\perp$, and adiabatic work $W_{\perp,\mathrm{ad}}$. (b) High-frequency electric field work. (c) Particle-averaged adiabatic moment $p_\perp{}^2/B$, scaled to the mean upstream value. (d) Magnetic field tilt $\psi = \tan^{-1}(B_x/\sqrt{B_y{}^2 + B_z{}^2})$ with respect to the y–z plane. Black curve is particle average $\langle\psi\rangle$; purple curves are 25th, 50th (median), and 75th percentiles. (e) Parallel, induction, ∇B, inertial, and polarization work. Dark-gray region is the error for sum of drift work; light-gray region is the error for $W_{\mathrm{tot,out}}$. (f) DC-like drift work, defined in the text. (g) Parallel work contributions from E_x, E_y, and E_z, as defined in the text. The y-axis is offset from (a)–(b) and (e)–(f).

$|E_\parallel|/(u_0 B_0/c) \sim 0.2$–$0.6$ and wavelength $\lambda_y \sim 2c/\omega_{\mathrm{pi}} \sim r_{\mathrm{Li}}$ (Figure 3(a), arrow); we attribute this $E_\parallel$ to very oblique whistler waves (i.e., magnetosonic/lower hybrid branch) with fluctuating $E_x \gg E_y$, E_z and B_y, $B_z > B_x$, as identified by prior PIC studies (Matsukiyo & Scholer 2003, 2006; Hellinger et al. 2007; Umeda et al. 2012b). A stronger bipolar ion-scale $|E_\parallel|/(u_0 B_0/c) \gtrsim 0.5$ (Figure 3(b), arrow) straddles clumps of shock-reflected ions and also accelerates electrons. Accelerated electrons appear as coherent deflections in $\gamma\beta_\parallel$–y phase space (Figures 3(g)–(h), arrows) that disrupt and relax via two-stream-like instability. Local y-regions develop asymmetric and transiently unstable $\gamma\beta_\parallel$ distributions (Figures 3(q), (v), (x)). Electron relaxation generates strong and rapid electron-scale $E_\parallel$ waves and phase-space holes with $\lambda_y \sim c/\omega_{\mathrm{pe}}$ (Figures 3(b), (g), (i), boxes; compare An et al. 2019) Landau damping is evidenced by flattened distributions at $\gamma\beta_\parallel \sim 0.2$ (Figures 3(k)–(l)). Electrons relax to near isotropy by $t' \sim 140\ \omega_{\mathrm{pi}}^{-1}$ (Figures 3(j), (o), (t), (y)). Prior 2D PIC simulations have shown similar two-step $\boldsymbol{B}$-parallel heating in a shock foot setup (periodic interpenetrating beams; Matsukiyo & Scholer 2006) and in full shocks (Umeda et al. 2011, 2012b).

$E_\parallel$ is the main source of non-adiabatic electron heating (Figure 4(a)). We decompose the sample electrons' mean energy gain W_{tot} into parallel and perpendicular work, $W_\parallel = -e\langle\int E_\parallel v_\parallel dt\rangle$ and $W_\perp = -e\langle\int E_\perp v_\perp dt\rangle$, integrated for every particle over every code time step Δt such that $W_{\mathrm{tot}} = W_\parallel + W_\perp$. Angle brackets are particle averages. We estimate the adiabatic heating as $W_{\perp,\mathrm{ad}} = \langle\sum_n(\gamma_{n\to n+1,\mathrm{ad}} - \gamma_n) m_{\mathrm{e}} c^2\rangle$, where

$$\gamma_{n\to n+1,\mathrm{ad}} = \sqrt{1 + (\gamma\beta_\parallel)_n^2 + (\gamma\beta_\perp)_n^2 (B_{n+1}/B_n)} \tag{1}$$

captures electron heating from compression between time steps n and $n+1$.

In Equation (1), we assume $(\gamma\beta_\perp)_n^2/B_n$ and $(\gamma\beta_\parallel)_n$ are constant during compression; γ, $\beta_\parallel$, and $\beta_\perp$ are evaluated in the electron fluid's rest frame. The sum in $W_{\perp,\mathrm{ad}}$ uses a coarse output time step $\Delta t_{\mathrm{out}} = 400\ \Delta t = 9\ \omega_{\mathrm{pe}}^{-1}$.

The non-adiabatic perpendicular work can be explained by high-frequency scattering of electron parallel energy into perpendicular energy (Figure 4(b)). We Fourier-space filter E_x, E_y, and E_z to isolate wavenumbers $k_y > (c/\omega_{\mathrm{pe}})^{-1}$ and then construct $E_{\perp,\mathrm{HF}}$ and $E_{\parallel,\mathrm{HF}}$ by projecting the Fourier-filtered fields onto local $\boldsymbol{B}$. Then, $W_{\perp,\mathrm{HF}} = -e\langle\sum E_{\perp,\mathrm{HF}} v_\perp \Delta t_{\mathrm{out}}\rangle$ and $W_{\parallel,\mathrm{HF}} = -e\langle\sum E_{\parallel,\mathrm{HF}} v_\parallel \Delta t_{\mathrm{out}}\rangle$. We find that $W_{\perp,\mathrm{HF}}$ and $W_\perp - W_{\perp,\mathrm{ad}}$ agree to $\sim$10%, suggesting that non-adiabatic $W_\perp$ comes from electron-scale scattering of parallel energy. Exact agreement is not expected due to the coarse time step Δt_{out} and the arbitrary k_y cut.

The particle-averaged adiabatic moment $p_\perp{}^2/B$ grows in steps that correlate with increases in W_{tot} and $W_\parallel$. Bulk acceleration at $t' = 84.6\ \omega_{\mathrm{pi}}^{-1}$ and $t' = 107.3\ \omega_{\mathrm{pi}}^{-1}$ coincides with momentarily constant $p_\perp{}^2/B$ and increasing $W_\parallel$ prior to a scattering episode. Then, $p_\perp{}^2/B$ increases during strong electron scattering at $t' = 89.6\ \omega_{\mathrm{pi}}^{-1}$ and $112.3\ \omega_{\mathrm{pi}}^{-1}$ while $W_\parallel$ flattens off (Figures 3 and 4(a), (c)).

Figure 4(e) shows mean work from grad B, inertial, and polarization drifts, as well as $\partial B/\partial t$ induction work; see Northrop (1961, 1963), Goodrich & Scudder (1984), Dahlin et al. (2014), and Rowan et al. (2019). Each $W_{\mathrm{drift}} = -e\langle\sum \boldsymbol{E}\cdot\boldsymbol{v}_{\mathrm{drift}}\Delta t_{\mathrm{out}}\rangle$, where $\boldsymbol{v}_{\mathrm{drift}}$ is one of

$$\boldsymbol{v}_{\{\nabla B,\mathrm{inert,pol}\}} = -\frac{\gamma m_{\mathrm{e}} c}{eB}\hat{\boldsymbol{b}} \times \left\{\frac{v_\perp{}^2}{2B}\nabla B,\ v_\parallel\frac{d\hat{\boldsymbol{b}}}{dt},\ \frac{d\boldsymbol{v}_E}{dt}\right\},$$

with γ and $v_\perp$ evaluated in the electron fluid's rest frame. We take $\boldsymbol{v}_E = \langle c\boldsymbol{E}\times\boldsymbol{B}/B^2\rangle$ to reduce noise; otherwise, the $\boldsymbol{v}_{\mathrm{drift}}$ terms use $\boldsymbol{E}$ and $\boldsymbol{B}$ fields seen by individual particles. The d/dt terms are one-sided finite differences, e.g., $d\boldsymbol{v}_E/dt = [(\boldsymbol{v}_E)_{n+1} - (\boldsymbol{v}_E)_n]/\Delta t_{\mathrm{out}}$. And, $W_{\mathrm{induct}} = \gamma m_{\mathrm{e}} v_\perp^2(\partial B/\partial t)/(2B)$, with $\partial B/\partial t = [B_{n+1}(\boldsymbol{r}_n) - B_{n-1}(\boldsymbol{r}_n)]/(2\Delta t_{\mathrm{out}})$ and $\boldsymbol{r}_n$ the particle position at time step n. We find that grad B drift and induction together give fluid-like adiabatic compression. Inertial and polarization drifts give less work, but some other electron samples have W_{inert} comparable to $W_{\nabla B}$ (Appendix A). We compare the summed drifts to $W_{\mathrm{tot,out}} = -e\langle\sum\boldsymbol{E}\cdot\boldsymbol{v}\Delta t_{\mathrm{out}}\rangle$. We conclude that W_{tot} agrees with both the summed drift work and $W_{\mathrm{tot,out}}$, given uncertainty from both the guiding-center drift approximation and the coarse integration time step.

Earlier, we argued that DC heating alone may not explain all super-adiabatic heating in our fiducial 2D shock, based on downstream volume-averaged $T_{\mathrm{e}}/T_{\mathrm{i}}$ (Figures 1(c) and 2(b)). So,

Figure 4(f) estimates DC-like work as $\overline{W}_{\rm drift} = -e\sum\langle \boldsymbol{E}\rangle \cdot \langle \boldsymbol{v}_{\rm drift}\rangle \Delta t_{\rm out}$ and $\overline{W}_{\parallel} = -e\sum\langle E_{\parallel}\rangle \langle v_{\parallel}\rangle \Delta t_{\rm out}$. The $\boldsymbol{E}$ average removes waves along $\hat{\boldsymbol{y}}$ to keep only 1D-like shock fields. The $\boldsymbol{v}_{\rm drift}$ average gives a mean drift trajectory and mostly discards gyration. The DC-like parallel work $\overline{W}_{\parallel}$ goes to zero, and the DC-like contribution to super-adiabatic heating appears small. Fluid-like adiabatic compression is preserved in $W_{\rm induct} + \overline{W}_{\nabla B}$. Figure 4(g) separates E_x, E_y, and E_z contributions to $W_{\parallel}$ as $W_{\parallel,Ei} = -e\langle \sum E_i b_i v_{\parallel} \Delta t_{\rm out}\rangle$, where $i = x, y, z$ and b_i is the ith component of $\hat{\boldsymbol{b}}$. E_y gives parallel heating, whereas E_x and E_z cause parallel cooling.

The quantities $W_{\perp,{\rm ad}}$, $W_{\{\parallel,\perp\},{\rm HF}}$, $W_{\rm drift}$, $W_{\rm tot,out}$, $\overline{W}_{\rm drift}$, $\overline{W}_{\parallel}$, and $W_{\parallel,Ei}$ are integrated with coarse time step $\Delta t_{\rm out}$ and converged at the ~10% level. The error regions in Figures 4(a), (b), (e) are defined in Appendix B.

5. Conclusion

We have measured $T_{\rm e}/T_{\rm i}$ in 2D PIC simulations of perpendicular shocks to inform models of astrophysical systems lacking direct $T_{\rm e}$ or $T_{\rm i}$ measurements. In a $\mathcal{M}_{\rm ms} = 3.1$, $\beta_{\rm p} = 0.25$ rippled shock, quasi-static DC fields provide fluid-like adiabatic heating, and most super-adiabatic heating is from ion-scale $E_{\parallel}$ waves.

Xinyi Guo shared and provided helpful assistance for some software used to perform and analyze these simulations. Alex Bergier and colleagues provided excellent assistance with Columbia's Habanero cluster. Adam Masters and Parviz Ghavamian kindly shared Saturn bow shock data. We thank Matthew W. Abruzzo, Luca Comisso, Greg Howes, Anatoly Spitkovsky, Vassilis Tsiolis, and Lynn B. Wilson III for discussion. We thank the anonymous referees for integral comments and critiques. L.S. and A.T. were supported by the Sloan Fellowship to L.S., NASA ATP-80NSSC20K0565, and NSF AST-1716567. Some work was done at UCSB KITP, which is supported by NSF PHY-1748958. Simulations were run on Habanero (Columbia University), Edison (NERSC), and Pleiades (NASA HEC). Columbia University's Shared Research Computing Facility is supported by NIH Research Facility Improvement grant 1G20RR030893-01 and the New York State Empire State Development, Division of Science Technology and Innovation (NYSTAR) Contract C090171. NERSC is a U.S. Department of Energy Office of Science User Facility operated under Contract DE-AC02-05CH11231. The NASA HEC Program is part of the NASA Advanced Supercomputing (NAS) Division at Ames Research Center.

Facilities: NERSC, Pleiades

Appendix A
More Views of Electron Sample Heating

Figures A1 and A2 present two animations of our electron sample traversing the shock front.

In Figure A3, we show the work decomposition from Figure 4 for many electron samples. At $t' = 0\ \omega_{\rm pi}^{-1}$, we selected all electrons in the regions $x \in [5.60, 5.62]c/\omega_{\rm pi}$, $x \in [6.00, 6.02]c/\omega_{\rm pi}$, and so on with even spacing $0.4c/\omega_{\rm pi}$ to get 17 electron particle samples of similar size.

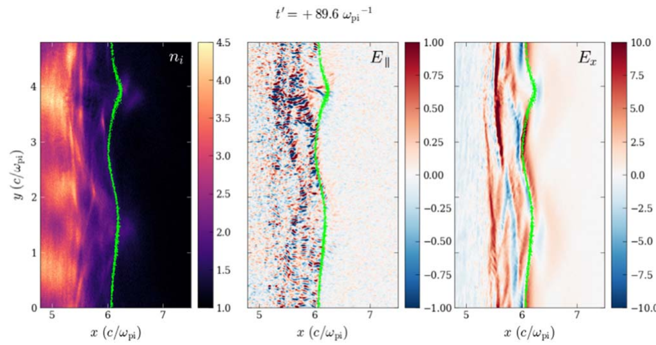

Figure A1. Animation still: electron sample at $t' = 89.6\ \omega_{\rm pi}^{-1}$ plotted over ion density $n_{\rm i}$, parallel electric field $E_{\parallel}$, and electric field component E_x; same sample from Figures 3 and 4. The animation of this figure spans $t' = 54$ to $180\ \omega_{\rm pi}^{-1}$. Its realtime duration is 23 s. The ion density $n_{\rm i}$ is scaled to upstream density n_0, and the electric field components are scaled to upstream motional electric field magnitude $u_0 B_0/c$. The $E_{\parallel}$ colormap spans $[-1, +1]$ and saturates on small-scale waves, despite being a wider range than Figure 3.

(An animation of this figure is available.)

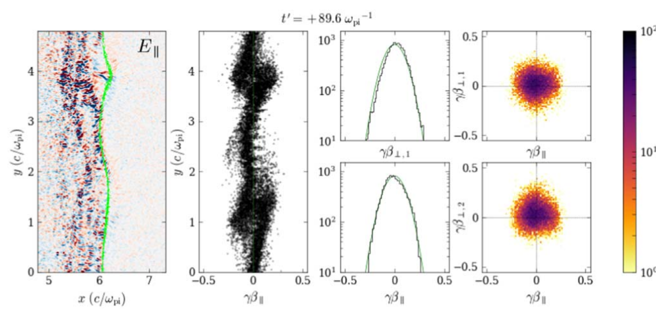

Figure A2. Animation still: electron sample phase space at $t' = 89.6\ \omega_{\rm pi}^{-1}$, with more detail than Figure 3. The animation of this figure spans $t' = 54$ to $180\ \omega_{\rm pi}^{-1}$. The animation's realtime duration is 23 s. The momentum component $\gamma\beta_{\perp,1}$ is the projection along $(\hat{\boldsymbol{b}} \times -\hat{\boldsymbol{x}}) \times \hat{\boldsymbol{b}}$, and the component $\gamma\beta_{\perp,2}$ is the projection along $\hat{\boldsymbol{b}} \times -\hat{\boldsymbol{x}}$. Because the local magnetic field unit vector $\hat{\boldsymbol{b}}$ mostly orients along $\hat{\boldsymbol{y}}$, the components $\perp$,1 and $\perp$,2 roughly correspond to $-\hat{\boldsymbol{x}}$ and $+\hat{\boldsymbol{z}}$ so that ($\perp$,1; $\perp$,2; $\parallel$) form a right-handed coordinate system. In the 1D phase-space plots, the light green curve is an isotropic Maxwell-Jüttner distribution with the same mean energy as the electrons. The $E_{\parallel}$ colormap is the same as in Figure A1.

(An animation of this figure is available.)

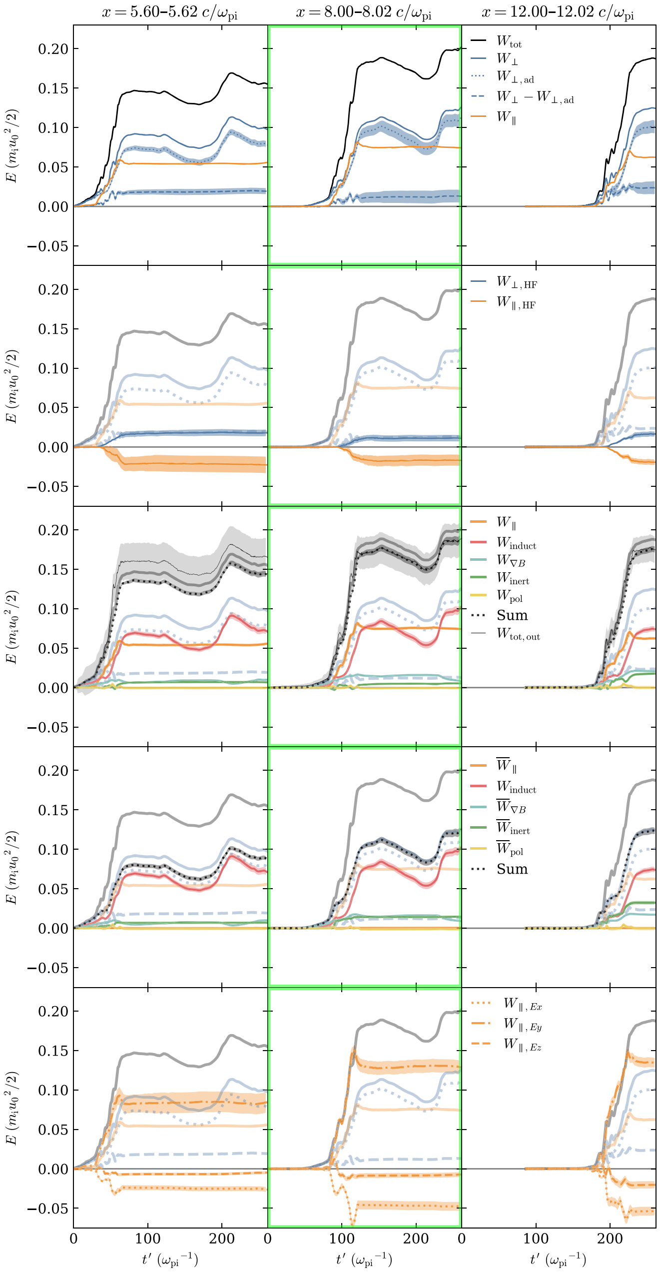

Figure A3. Like Figures 4(a)–(b), (e)–(g), but for multiple electron samples traversing the shock at different times. Left and right: first and last samples tracked. Middle (green box): sample shown in Figures 3 and 4. Column titles indicate the sample's location at $t' = 0\quad \omega_{pi}^{-1}$.

(The complete figure set (17 images) is available.)

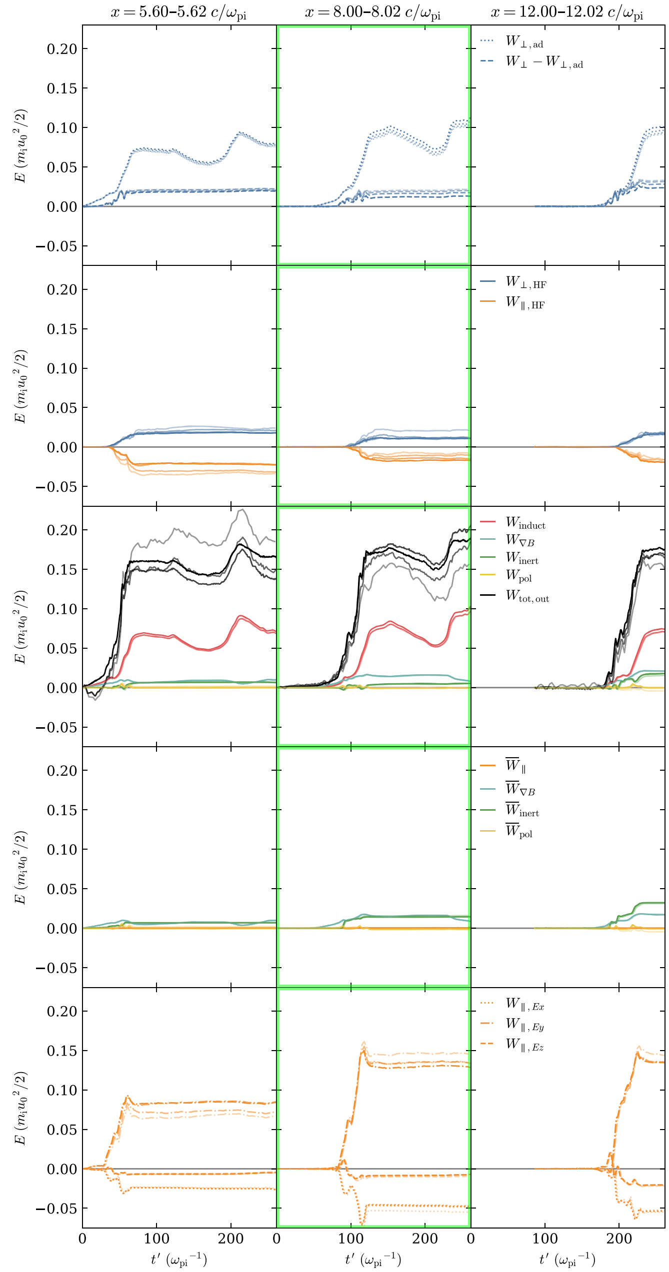

Figure B1. Like Figure A3, but showing the numerical convergence of all quantities integrated with the coarse time step Δt_{out}, listed in the text. For each quantity, we increase the sample spacing Δt_{out} by 2×, 4×, and 8× and plot the downsampled integration with progressively decreasing opacity.

(The complete figure set (17 images) is available.)

Appendix B
Convergence in Electron Work Summation

Several quantities in Figure 4 are summed with a coarse time step $\Delta t_{out} = 400\Delta t = 9\,\omega_{pe}^{-1}$, namely: $W_{\perp,ad}$, $W_\perp - W_{\perp,ad}$, $W_{\perp,HF}$, $W_{\parallel,HF}$, W_{induct}, $W_{\nabla B}$, W_{inert}, W_{pol}, $W_{tot,out}$, $\overline{W}_{\nabla B}$, $\overline{W}_{inert}$, $\overline{W}_{pol}$, $\overline{W}_\parallel$, $W_{\parallel,Ex}$, $W_{\parallel,Ey}$, and $W_{\parallel,Ez}$. To check convergence, we downsample in time each quantity's summand by 4 and compute an error δf at discrete time t_n as

$$\delta f(t_n) = \max\{|f(t_m) - f_{1/4}(t_m)|\,|\,0 \leqslant m \leqslant n\}, \qquad \text{(B1)}$$

where $f_{1/4}$ is the 4× downsampled version of f. Thus δf is strictly non-decreasing with t_n. The error regions defined by Equation (B1) are plotted as shaded areas in Figures 4 and A3.

Figure B1 shows curves with 2×, 4×, 8× downsampling for the 17 distinct electron samples of Figure A3, including the sample shown in Figure 4.

Appendix C
Transverse Width Convergence

Figure C1 shows that our fiducial 2D simulations are converged with respect to transverse width. Most of the varying

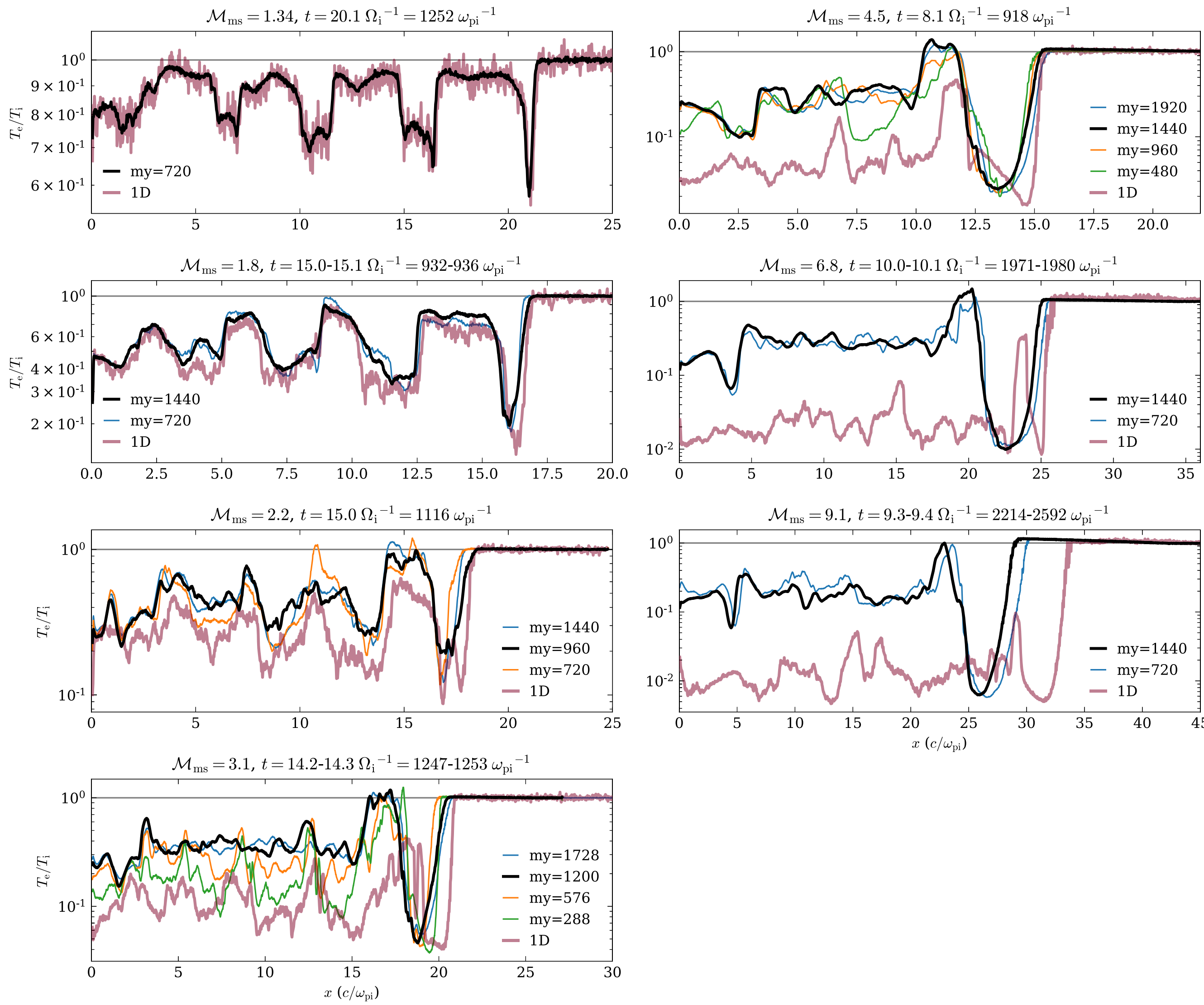

Figure C1. Fiducial 2D simulations are converged with respect to transverse width. Black curves are fiducial 2D $m_i/m_e = 625$, $\beta_p = 0.25$ simulations from Figure 2(a). Colored curves are the same shock parameters with varying input `my`, as defined in Appendix D. A time range is given because simulation output times do not match exactly.

transverse width simulations are *not* listed in Table D1. For $\mathcal{M}_{ms} = 9.1$ only, the 1D simulation uses a slightly higher upstream temperature than the 2D simulations, so the ratio Ω_i/ω_{pi} differs between 1D and 2D. In this case, we matched times based on Ω_i^{-1} rather than ω_{pi}^{-1}.

Appendix D
Simulation Parameters

Table D1 contains input parameters, derived shock parameters, run durations, and downstream temperature measurements for all simulations in our Letter. The first row is the high-resolution run used in Figures 3 and 4; the remaining rows are presented in Figure 2. A machine-readable version of Table D1, in comma-separated value (CSV) ASCII, is available. Below, we define all table columns.

1. `mi_me` is the ion–electron mass ratio m_i/m_e.
2. `theta` and `phi` specify the upstream magnetic field orientation, measured in the simulation frame. θ is the angle between $\boldsymbol{B}$ and the x-coordinate axis. φ is the angle between the y–z plane projection of $\boldsymbol{B}$ and the z-coordinate axis. To visualize these angles, see Figure 1 of Guo et al. (2014), but note that their $\varphi_B = \pi/2 - \varphi$ is the complement of our φ. For all our simulations, θ corresponds to the angle between $\boldsymbol{B}$ and shock normal. The 2D simulations with in-plane $\boldsymbol{B}$ have $\theta = 90°$ and $\varphi = 90°$. The 2D simulations with out-of-plane $\boldsymbol{B}$ (i.e., $\boldsymbol{B}$ along $\hat{z}$) have $\theta = 90°$ and $\varphi = 0°$. The 1D simulations with oblique $\boldsymbol{B}$ have have $\theta < 90°$.
3. `my` and `mz` are the numbers of grid cells along $\hat{y}$ and $\hat{z}$. Our 2D simulations have `mz` $= 1$, and 1D simulations have `my` $=$ `mz` $= 1$.
4. `betap`, `Ms`, `Ma`, and `Mms` are the shock plasma beta β_p, sonic Mach number $\mathcal{M}_s$, Alfvén Mach number $\mathcal{M}_A$, and fast magnetosonic Mach number $\mathcal{M}_{ms}$. These numbers are *derived* from TRISTAN-MP input parameters `sigma`, `delgam`, and `u0` (defined just below). First, the total plasma beta is

$$\beta_p = \frac{4\gamma_0 \Delta\gamma_i}{\sigma(\gamma_0 - 1)(1 + m_e/m_i)},$$

Table D1

Simulation Input Parameters, Derived Shock Parameters, Run Duration, and Downstream Temperature Measurements; Columns Are Defined in Appendix D

mi_me	theta	phi	my	mz	betap	Ms	Ma	Mms	sigma	delgam	u0	ppc0	c_omp	ntimes	dur	Te_Ti	Te_Ti_std	Te	Ti
625	90	90	2400	1	0.250	6.86	3.43	3.07	4.7854E−1	8.0944E−6	2.3245E−2	128	20	64	6.7	⋯	⋯	⋯	⋯
625	90	90	720	1	0.251	3.00	1.50	1.34	1.0117E+1	1.6189E−5	7.1502E−3	32	10	32	20.1	8.53E−1	1.38E−1	1.29E−2	2.43E−5
625	90	90	1440	1	0.250	4.00	2.00	1.79	2.3774E+0	1.6189E−5	1.4749E−2	32	10	32	15.0	5.59E−1	2.33E−1	1.74E−2	4.96E−5
625	90	90	960	1	0.250	5.00	2.50	2.24	1.1237E+0	1.1332E−5	1.7949E−2	32	10	32	20.1	4.52E−1	1.69E−1	1.96E−2	6.92E−5
625	90	90	1200	1	0.250	6.86	3.43	3.07	4.7854E−1	8.0944E−6	2.3245E−2	32	10	32	14.2	3.65E−1	1.28E−1	2.83E−2	1.24E−4
625	90	90	1440	1	0.250	9.99	4.99	4.47	1.9968E−1	4.8566E−6	2.7873E−2	32	10	32	12.1	3.18E−1	1.22E−1	3.65E−2	1.83E−4
625	90	90	1440	1	0.250	15.19	7.60	6.79	8.1402E−2	1.6189E−6	2.5205E−2	32	10	32	10.0	2.97E−1	1.22E−1	2.80E−2	1.51E−4
625	90	90	1440	1	0.250	20.37	10.18	9.11	4.4398E−2	8.0944E−7	2.4133E−2	32	10	32	9.8	1.98E−1	5.99E−2	1.83E−2	1.47E−4
625	90	0	1440	1	0.251	3.00	1.50	1.34	1.0117E+1	1.6189E−5	7.1502E−3	32	10	32	19.0	8.62E−1	1.20E−1	1.30E−2	2.42E−5
625	90	0	1440	1	0.250	4.00	2.00	1.79	2.3774E+0	1.6189E−5	1.4749E−2	32	10	32	19.9	4.71E−1	1.78E−1	1.60E−2	5.42E−5
625	90	0	1440	1	0.250	5.00	2.50	2.24	1.1237E+0	1.1332E−5	1.7949E−2	32	10	32	15.0	2.49E−1	1.28E−1	1.24E−2	7.93E−5
625	90	0	1440	1	0.250	7.00	3.50	3.13	4.5493E−1	8.0944E−6	2.3840E−2	32	10	32	15.2	1.07E−1	5.45E−2	1.02E−2	1.54E−4
625	90	0	1440	1	0.250	10.00	5.00	4.47	1.9912E−1	4.8566E−6	2.7912E−2	32	10	32	9.8	4.48E−2	2.30E−2	6.82E−3	2.44E−4
625	90	0	1440	1	0.250	15.00	7.50	6.71	8.3580E−2	1.6189E−6	2.4874E−2	32	10	32	8.5	2.54E−2	2.43E−2	3.11E−3	1.96E−4
625	90	90	1	1	0.251	3.00	1.50	1.34	1.0117E+1	1.6189E−5	7.1502E−3	512	10	32	40.0	8.52E−1	1.05E−1	1.32E−2	2.47E−5
625	90	90	1	1	0.250	4.00	2.00	1.79	2.3774E+0	1.6189E−5	1.4749E−2	512	10	32	40.0	4.28E−1	1.86E−1	1.58E−2	5.92E−5
625	90	90	1	1	0.250	5.00	2.50	2.24	1.1237E+0	1.1332E−5	1.7949E−2	512	10	32	25.2	2.36E−1	8.40E−2	1.24E−2	8.40E−5
625	90	90	1	1	0.250	7.00	3.50	3.13	4.5493E−1	8.0944E−6	2.3840E−2	512	10	32	25.0	1.01E−1	3.87E−2	1.02E−2	1.61E−4
625	90	90	1	1	0.250	10.00	5.00	4.47	1.9912E−1	4.8566E−6	2.7912E−2	512	10	32	15.2	5.02E−2	3.44E−2	7.03E−3	2.24E−4
625	90	90	1	1	0.250	15.00	7.50	6.71	8.3580E−2	1.6189E−6	2.4874E−2	1024	10	32	15.1	2.38E−2	1.57E−2	2.85E−3	1.92E−4
625	90	90	1	1	0.250	20.00	10.00	8.94	4.6080E−2	1.1332E−6	2.8027E−2	2048	10	32	10.1	1.35E−2	1.18E−2	2.05E−3	2.43E−4
625	85	90	1	1	0.251	3.00	1.50	1.34	1.0117E+1	1.6189E−5	7.1502E−3	2048	10	64	40.0	9.15E−1	7.96E−2	1.36E−2	2.38E−5
625	85	90	1	1	0.250	4.00	2.00	1.79	2.3774E+0	1.6189E−5	1.4749E−2	2048	10	64	40.0	4.91E−1	1.61E−1	1.70E−2	5.54E−5
625	85	90	1	1	0.250	5.00	2.50	2.23	1.1237E+0	1.1332E−5	1.7949E−2	2048	10	64	25.2	2.79E−1	1.57E−1	1.36E−2	7.79E−5
625	85	90	1	1	0.250	7.00	3.50	3.13	4.5493E−1	8.0944E−6	2.3840E−2	2048	10	64	20.0	1.35E−1	4.98E−2	1.35E−2	1.60E−4
625	85	90	1	1	0.250	10.00	5.00	4.47	1.9912E−1	4.8566E−6	2.7912E−2	2048	10	64	15.2	1.29E−1	3.69E−2	1.75E−2	2.17E−4
625	80	90	1	1	0.251	2.99	1.50	1.34	1.0117E+1	1.6189E−5	7.1502E−3	2048	10	64	30.1	8.73E−1	4.51E−2	1.27E−2	2.32E−5
625	80	90	1	1	0.250	3.99	2.00	1.79	2.3774E+0	1.6189E−5	1.4749E−2	2048	10	64	30.1	6.58E−1	1.09E−1	1.94E−2	4.72E−5
625	80	90	1	1	0.250	4.99	2.50	2.23	1.1237E+0	1.1332E−5	1.7949E−2	2048	10	64	25.2	5.28E−1	1.62E−1	2.13E−2	6.45E−5
625	80	90	1	1	0.250	6.99	3.49	3.13	4.5493E−1	8.0944E−6	2.3840E−2	2048	10	64	20.0	2.38E−1	1.27E−1	2.05E−2	1.38E−4
625	80	90	1	1	0.250	9.99	5.00	4.47	1.9912E−1	4.8566E−6	2.7912E−2	2048	10	64	15.2	1.89E−1	8.87E−2	2.27E−2	1.91E−4
625	75	90	1	1	0.251	2.98	1.49	1.34	1.0117E+1	1.6189E−5	7.1502E−3	2048	10	64	40.0	8.54E−1	2.44E−2	1.27E−2	2.37E−5
625	75	90	1	1	0.250	3.98	1.99	1.78	2.3774E+0	1.6189E−5	1.4749E−2	2048	10	64	30.1	6.45E−1	7.82E−2	1.94E−2	4.80E−5
625	75	90	1	1	0.250	4.98	2.49	2.23	1.1237E+0	1.1332E−5	1.7949E−2	2048	10	64	25.2	7.76E−1	1.81E−1	2.69E−2	5.55E−5
625	75	90	1	1	0.250	6.98	3.49	3.12	4.5493E−1	8.0944E−6	2.3840E−2	2048	10	64	20.0	1.11E+0	1.90E−1	5.52E−2	7.95E−5
625	75	90	1	1	0.250	9.98	4.99	4.46	1.9912E−1	4.8566E−6	2.7912E−2	2048	10	64	15.2	2.58E−1	1.27E−1	3.09E−2	1.92E−4
20	90	90	720	1	0.250	3.00	1.50	1.34	9.8755E+0	5.0590E−4	3.9505E−2	32	10	32	39.2	8.62E−1	9.55E−2	1.29E−2	7.46E−4
20	90	90	720	1	0.250	4.00	2.00	1.79	2.2975E+0	5.0590E−4	8.1851E−2	32	10	32	39.2	4.43E−1	1.69E−1	1.58E−2	1.79E−3
20	90	90	720	1	0.250	5.00	2.50	2.24	1.0872E+0	3.5413E−4	9.9512E−2	32	10	32	29.5	2.83E−1	1.40E−1	1.38E−2	2.44E−3
20	90	90	720	1	0.250	6.84	3.42	3.06	4.6363E−1	2.5295E−4	1.2868E−1	32	10	32	24.5	2.13E−1	8.37E−2	1.73E−2	4.07E−3
20	90	90	720	1	0.250	9.93	4.97	4.44	1.9289E−1	1.5177E−4	1.5439E−1	32	10	32	19.6	1.85E−1	8.66E−2	2.34E−2	6.33E−3
20	90	90	720	1	0.250	15.12	7.56	6.76	7.9463E−2	5.0590E−5	1.3896E−1	32	10	32	14.7	1.70E−1	4.14E−2	1.82E−2	5.36E−3
20	90	90	960	1	0.250	20.27	10.14	9.07	4.3483E−2	2.5295E−5	1.3285E−1	32	10	32	14.7	1.64E−1	4.36E−2	1.69E−2	5.15E−3

Table D1
(Continued)

mi_me	theta	phi	my	mz	betap	Ms	Ma	Mms	sigma	delgam	u0	ppc0	c_omp	ntimes	dur	Te_Ti	Te_Ti_std	Te	Ti
49	90	90	1440	1	0.250	3.00	1.50	1.34	1.0020E+1	2.0649E−4	2.5420E−2	32	10	32	39.5	8.53E−1	1.09E−1	1.28E−2	3.07E−4
49	90	90	1440	1	0.250	4.00	2.00	1.79	2.3453E+0	2.0649E−4	5.2528E−2	32	10	32	39.5	4.78E−1	2.11E−1	1.59E−2	6.78E−4
49	90	90	1440	1	0.250	5.00	2.50	2.24	1.1090E+0	1.4454E−4	6.3899E−2	32	10	32	25.0	3.37E−1	1.71E−1	1.54E−2	9.32E−4
49	90	90	1440	1	0.250	6.85	3.42	3.06	4.7256E−1	1.0325E−4	8.2703E−2	32	10	32	25.6	3.26E−1	1.43E−1	2.35E−2	1.47E−3
49	90	90	1440	1	0.250	9.97	4.98	4.46	1.9696E−1	6.1947E−5	9.9192E−2	32	10	32	25.0	2.75E−1	6.97E−2	3.22E−2	2.39E−3
49	90	90	720	1	0.250	15.16	7.58	6.78	8.0625E−2	2.0649E−5	8.9530E−2	128	10	32	15.0	1.81E−1	4.46E−2	1.92E−2	2.16E−3
49	90	90	720	1	0.250	20.33	10.17	9.09	4.4032E−2	1.0325E−5	8.5672E−2	128	10	32	14.9	1.32E−1	3.76E−2	1.42E−2	2.19E−3
49	90	90	360	1	0.250	30.63	15.32	13.70	1.9157E−2	4.1298E−6	8.2153E−2	128	10	32	10.0	1.14E−1	3.67E−2	1.11E−2	1.97E−3
200	90	90	1440	1	0.250	3.00	1.50	1.34	1.0099E+1	5.0590E−5	1.2629E−2	32	10	32	33.1	8.54E−1	1.16E−1	1.28E−2	7.49E−5
200	90	90	1440	1	0.250	4.00	2.00	1.79	2.3715E+0	5.0590E−5	2.6060E−2	32	10	32	39.3	5.40E−1	2.04E−1	1.80E−2	1.66E−4
200	90	90	1440	1	0.250	5.00	2.50	2.24	1.1210E+0	3.5413E−5	3.1711E−2	32	10	32	29.0	4.75E−1	2.00E−1	2.03E−2	2.14E−4
200	90	90	1440	1	0.250	6.86	3.43	3.07	4.7744E−1	2.5295E−5	4.1064E−2	32	10	32	21.5	3.66E−1	1.52E−1	2.67E−2	3.65E−4
200	90	90	1440	1	0.250	9.98	4.99	4.46	1.9918E−1	1.5177E−5	4.9241E−2	32	10	32	20.0	3.73E−1	1.16E−1	3.91E−2	5.24E−4
200	90	90	1440	1	0.250	15.18	7.59	6.79	8.1259E−2	5.0590E−6	4.4512E−2	32	10	32	15.0	2.44E−1	7.44E−2	2.51E−2	5.14E−4
200	90	90	1440	1	0.250	20.36	10.18	9.11	4.4331E−2	2.5295E−6	4.2614E−2	64	10	32	10.2	1.51E−1	6.25E−2	1.55E−2	5.13E−4
49	90	90	192	192	0.250	4.00	2.00	1.79	2.3453E+0	2.0649E−4	5.2528E−2	32	10	32	24.1	4.65E−1	2.23E−1	1.57E−2	6.90E−4
49	90	90	192	192	0.250	5.00	2.50	2.24	1.1090E+0	1.4454E−4	6.3899E−2	32	10	32	35.3	3.37E−1	2.07E−1	1.57E−2	9.54E−4
49	90	90	192	384	0.250	6.85	3.42	3.06	4.7256E−1	1.0325E−4	8.2703E−2	32	10	32	17.4	2.74E−1	1.40E−1	2.12E−2	1.58E−3
49	90	90	192	192	0.250	9.97	4.98	4.46	1.9696E−1	6.1947E−5	9.9192E−2	32	10	32	15.0	2.37E−1	1.61E−1	2.84E−2	2.45E−3
49	90	90	192	192	0.250	15.16	7.58	6.78	8.0625E−2	2.0649E−5	8.9530E−2	32	10	32	8.9	1.50E−1	7.62E−2	1.58E−2	2.16E−3
49	90	90	1440	1	0.125	4.00	1.41	1.33	1.1537E+1	2.0649E−4	3.3500E−2	32	10	32	24.8	7.71E−1	1.32E−1	1.28E−2	3.38E−4
49	90	90	1440	1	0.125	5.00	1.77	1.67	3.4565E+0	1.4454E−4	5.1197E−2	32	10	32	24.8	4.14E−1	1.98E−1	1.06E−2	5.22E−4
49	90	90	1440	1	0.125	6.68	2.36	2.23	1.2431E+0	1.0325E−4	7.2128E−2	32	10	32	25.0	2.42E−1	1.35E−1	1.14E−2	9.66E−4
49	90	90	1440	1	0.125	9.78	3.46	3.26	4.4927E−1	6.1947E−5	9.2894E−2	32	10	32	24.8	3.09E−1	1.34E−1	2.68E−2	1.77E−3
49	90	90	1440	1	0.125	14.99	5.30	5.00	1.7122E−1	2.0649E−5	8.6888E−2	32	10	32	20.1	2.65E−1	8.51E−2	2.32E−2	1.79E−3
49	90	90	1440	1	0.125	20.19	7.14	6.73	9.1148E−2	1.0325E−5	8.4213E−2	32	10	32	15.1	2.10E−1	6.01E−2	1.88E−2	1.83E−3
49	90	90	360	1	0.125	30.53	10.79	10.18	3.8916E−2	4.1298E−6	8.1516E−2	128	10	32	10.1	1.47E−1	8.28E−2	1.36E−2	1.89E−3
49	90	90	720	1	0.500	2.00	1.41	1.15	3.5805E+1	2.0649E−4	9.5092E−3	32	10	32	38.8	9.95E−1	6.62E−2	1.14E−2	2.34E−4
49	90	90	1440	1	0.500	3.00	2.12	1.73	2.2310E+0	2.0649E−4	3.8088E−2	32	10	32	38.8	6.17E−1	1.70E−1	1.54E−2	5.09E−4
49	90	90	1440	1	0.500	3.87	2.74	2.24	9.2639E−1	2.0649E−4	5.9093E−2	32	10	32	25.9	3.99E−1	1.41E−1	1.93E−2	9.85E−4
49	90	90	1440	1	0.500	4.90	3.47	2.83	4.8236E−1	1.4454E−4	6.8506E−2	32	10	32	26.0	4.00E−1	1.29E−1	2.30E−2	1.17E−3
49	90	90	1440	1	0.500	6.98	4.93	4.03	2.0639E−1	1.0325E−4	8.8477E−2	32	10	32	25.6	2.80E−1	5.22E−2	2.81E−2	2.04E−3
49	90	90	1440	1	0.500	10.08	7.13	5.82	9.2084E−2	6.1947E−5	1.0257E−1	32	10	32	25.5	2.05E−1	3.55E−2	2.94E−2	2.94E−3
49	90	90	1440	1	0.500	15.26	10.79	8.81	3.9095E−2	2.0649E−5	9.0910E−2	32	10	32	19.9	1.47E−1	1.99E−2	1.78E−2	2.47E−3
49	90	90	1440	1	1.000	2.00	2.00	1.41	4.4802E+0	2.0649E−4	1.9008E−2	32	10	32	25.0	9.19E−1	1.39E−1	1.34E−2	2.97E−4
49	90	90	1440	1	1.000	3.00	3.00	2.12	8.2034E−1	2.0649E−4	4.4412E−2	32	10	32	25.0	5.18E−1	1.55E−1	1.76E−2	6.95E−4
49	90	90	1440	1	1.000	4.00	4.00	2.83	3.6299E−1	2.0649E−4	6.6745E−2	32	10	32	25.0	3.64E−1	1.08E−1	2.37E−2	1.33E−3
49	90	90	1440	1	1.000	4.99	4.99	3.53	2.1083E−1	1.4454E−4	7.3265E−2	32	10	32	24.8	3.42E−1	8.28E−2	2.55E−2	1.52E−3
49	90	90	1440	1	1.000	7.06	7.06	4.99	9.6333E−2	1.0325E−4	9.1569E−2	32	10	32	24.8	2.18E−1	3.84E−2	2.54E−2	2.37E−3
49	90	90	1440	1	1.000	10.15	10.15	7.18	4.4490E−2	6.1947E−5	1.0434E−1	32	10	32	25.0	1.59E−1	2.53E−2	2.49E−2	3.19E−3
49	90	90	1440	1	1.000	15.31	15.31	10.82	1.9246E−2	2.0649E−5	9.1619E−2	32	10	32	24.8	1.32E−1	1.91E−2	1.64E−2	2.53E−3
49	90	90	1440	1	2.000	2.00	2.83	1.63	1.4344E+0	2.0649E−4	2.3754E−2	32	10	32	24.8	8.56E−1	1.86E−1	1.50E−2	3.58E−4
49	90	90	1440	1	2.000	3.00	4.24	2.45	3.5747E−1	2.0649E−4	4.7572E−2	32	10	32	24.8	5.24E−1	9.73E−2	2.04E−2	7.93E−4
49	90	90	1512	1	2.000	4.00	5.66	3.27	1.6927E−1	2.0649E−4	6.9110E−2	32	10	32	27.8	3.39E−1	4.34E−2	2.63E−2	1.59E−3

Table D1
(Continued)

mi_me	theta	phi	my	mz	betap	Ms	Ma	Mms	sigma	delgam	u0	ppc0	c_omp	ntimes	dur	Te_Ti	Te_Ti_std	Te	Ti
49	90	90	1512	1	2.000	5.00	7.07	4.08	1.0012E−1	2.0649E−4	8.9824E−2	32	10	32	24.6	2.58E−1	3.86E−2	3.21E−2	2.55E−3
49	90	90	1440	1	2.000	7.11	10.05	5.80	4.6506E−2	1.0325E−4	9.3186E−2	32	10	32	24.9	1.86E−1	2.32E−2	2.42E−2	2.66E−3
49	90	90	2016	1	2.000	10.19	14.41	8.32	2.1861E−2	6.1947E−5	1.0525E−1	32	10	32	18.8	1.33E−1	1.29E−2	2.26E−2	3.46E−3
49	90	90	1440	1	2.000	15.33	21.69	12.52	9.5477E−3	2.0649E−5	9.1978E−2	32	10	32	12.0	1.22E−1	2.36E−2	1.57E−2	2.63E−3
49	90	90	1440	1	4.000	2.00	4.00	1.79	5.9285E−1	2.0649E−4	2.6126E−2	32	10	32	25.1	8.35E−1	1.87E−1	1.62E−2	3.96E−4
49	90	90	1512	1	4.000	3.00	6.00	2.68	1.6743E−1	2.0649E−4	4.9151E−2	32	10	32	23.8	4.90E−1	6.76E−2	2.21E−2	9.19E−4
49	90	90	1512	1	4.000	4.00	8.00	3.58	8.1810E−2	2.0649E−4	7.0292E−2	32	10	32	34.3	3.45E−1	4.17E−2	2.79E−2	1.65E−3
49	90	90	1512	1	4.000	5.00	10.00	4.47	4.9023E−2	2.0649E−4	9.0767E−2	32	10	32	36.6	2.60E−1	2.30E−2	3.32E−2	2.61E−3
49	90	90	1440	1	4.000	7.13	14.27	6.38	2.2843E−2	1.0325E−4	9.4017E−2	32	10	32	25.1	1.69E−1	1.46E−2	2.31E−2	2.79E−3
49	90	90	2160	1	4.000	10.21	20.42	9.13	1.0835E−2	6.1947E−5	1.0571E−1	32	10	32	19.0	1.35E−1	1.22E−2	2.33E−2	3.52E−3

(This table is available in its entirety in machine-readable form.)

where $\gamma_0 = 1/\sqrt{1-(u_0/c)^2}$ is the Lorentz factor of the upstream flow in the simulation frame. The sonic Mach number depends on the upstream plasma speed in the shock's rest frame:

$$\mathcal{M}_s = \frac{u_{sh}}{c_s} = \frac{u_0}{(1 - 1/r(\mathcal{M}_s))c_s},$$

and we solve this implicit expression for $\mathcal{M}_s$ (and thus also u_{sh}) using an input u_0 and assumed fluid adiabatic index $\Gamma = 2$ (note that Γ enters into both the Rankine–Hugoniot expression for MHD shock-compression ratio r and the sound speed c_s). Once $\mathcal{M}_s$ and u_{sh} are known, $\mathcal{M}_A$ and $\mathcal{M}_{ms}$ are known as well. This procedure for estimating shock parameters is taken directly from Guo et al. (2017).

5. `sigma` is the magnetization, a ratio of upstream magnetic and kinetic enthalpy densities:

$$\texttt{sigma} = \sigma \equiv \frac{{B_0}^2}{4\pi(\gamma_0 - 1)(m_i + m_e)n_0 c^2}.$$

6. `delgam` is the upstream plasma temperature, in units of ion rest mass energy:

$$\texttt{delgam} = \Delta\gamma_i \equiv \frac{k_B T_0}{m_i c^2}.$$

7. `u0` is the upstream plasma velocity, in units of speed of light:

$$\texttt{u0} \equiv u_0/c.$$

8. `ppc0` is number of particles (both electrons and ions) per cell in the upstream plasma.
9. `c_omp` is the number of grid cells per electron skin depth c/ω_{pe}.
10. `ntimes` is the number of current filter passes.
11. `dur` is the simulation duration in units of upstream inverse ion cyclotron frequency Ω_i^{-1}.
12. `Te_Ti` is our measurement of downstream temperature ratio T_e/T_i. As described in the main text, we manually choose a downstream region that is minimally affected by the left-side reflecting wall and the right-side shock front relaxation. Our measurement of T_e/T_i uses downsampled grid output of the particle temperature tensor; however, the temperature tensor itself is calculated for each grid cell using the full particle distribution in a 5^N cell region, where $N \in \{1, 2, 3\}$ is the domain dimensionality.
13. `Te_Ti_std` is the standard deviation of T_e/T_i within the downstream region that we consider. Like `Te_Ti`, downsampled grid output is used for this estimate.
14. `Te` and `Ti` are the downstream electron and ion temperatures scaled to their respective rest mass energies, i.e., $k_B T_e/(m_e c^2)$ and $k_B T_i/(m_i c^2)$. We measure all of `Te`, `Ti`, and `Te_Ti` in the same manually chosen downstream region.

ORCID iDs

Aaron Tran https://orcid.org/0000-0003-3483-4890
Lorenzo Sironi https://orcid.org/0000-0002-5951-0756

References

An, X., Li, J., Bortnik, J., et al. 2019, PhRvL, 122, 045101
Avestruz, C., Nagai, D., Lau, E. T., & Nelson, K. 2015, ApJ, 808, 176
Birdsall, C. K., & Langdon, A. B. 1991, Plasma Physics via Computer Simulation, The Adam Hilger Series on Plasma Physics (Bristol: IOP Publishing)
Buneman, O. 1993, in Computer Space Plasma Physics: Simulation Techniques and Software, ed. H. Matsumoto & Y. Omura (Tokyo: Terra Scientific), 67
Chen, L.-J., Wang, S., Wilson, L. B., III, et al. 2018, PhRvL, 120, 225101
Cohen, I. J., Schwartz, S. J., Goodrich, K. A., et al. 2019, JGRA, 124, 3961
Dahlin, J. T., Drake, J. F., & Swisdak, M. 2014, PhPl, 21, 092304
Dimmock, A. P., Russell, C. T., Sagdeev, R. Z., et al. 2019, SciA, 5, eaau9926
Feldman, W. C., Anderson, R. C., Bame, S. J., et al. 1983, JGR, 88, 96
Feldman, W. C., Bame, S. J., Gary, S. P., et al. 1982, PhRvL, 49, 199
Ghavamian, P., Schwartz, S. J., Mitchell, J., Masters, A., & Laming, J. M. 2013, SSRv, 178, 633
Goodrich, C. C., & Scudder, J. D. 1984, JGR, 89, 6654
Goodrich, K. A., Ergun, R., Schwartz, S. J., et al. 2018, JGRA, 123, 9430
Guo, X., Sironi, L., & Narayan, R. 2014, ApJ, 794, 153
Guo, X., Sironi, L., & Narayan, R. 2017, ApJ, 851, 134
Guo, X., Sironi, L., & Narayan, R. 2018, ApJ, 858, 95
Hanson, E. L. M., Agapitov, O. V., Mozer, F. S., et al. 2019, GeoRL, 46, 2381
Helder, E. A., Kosenko, D., & Vink, J. 2010, ApJL, 719, L140
Hellinger, P., Trávníček, P., Lembège, B., & Savoini, P. 2007, GeoRL, 34, L14109
Hovey, L., Hughes, J. P., McCully, C., Pandya, V., & Eriksen, K. 2018, ApJ, 862, 148
Hull, A. J., Scudder, J. D., Larson, D. E., & Lin, R. 2001, JGR, 106, 15711
Johlander, A., Schwartz, S. J., Vaivads, A., et al. 2016, PhRvL, 117, 165101
Krasnoselskikh, V. V., Lembège, B., Savoini, P., & Lobzin, V. V. 2002, PhPl, 9, 1192
Krauss-Varban, D., Pantellini, F. G. E., & Burgess, D. 1995, GeoRL, 22, 2091
Lefebvre, B., Schwartz, S. J., Fazakerley, A. F., & Décréau, P. 2007, JGRA, 112, A09212
Leroy, M. M., Winske, D., Goodrich, C. C., Wu, C. S., & Papadopoulos, K. 1982, JGR, 87, 5081
Lowe, R. E., & Burgess, D. 2003, AnGeo, 21, 671
Masters, A., Schwartz, S. J., Henley, E. M., et al. 2011, JGRA, 116, A10107
Matsukiyo, S., & Scholer, M. 2003, JGRA, 108, 1459
Matsukiyo, S., & Scholer, M. 2006, JGRA, 111, A06104
Muschietti, L., & Lembège, B. 2017, AnGeo, 35, 1093
Northrop, T. G. 1961, AnPhy, 15, 79
Northrop, T. G. 1963, RvGSP, 1, 283
Richardson, J. D. 2002, P&SS, 50, 503
Rowan, M. E., Sironi, L., & Narayan, R. 2019, ApJ, 873, 2
Schwartz, S. J. 2014, JGRA, 119, 1507
Schwartz, S. J., Thomsen, M. F., Bame, S. J., & Stansberry, J. 1988, JGR, 93, 12923
Scudder, J. D. 1996, JGR, 101, 2561
Scudder, J. D., Mangeney, A., Lacombe, C., et al. 1986, JGR, 91, 11075
Shimada, N., & Hoshino, M. 2000, ApJL, 543, L67
Shimada, N., & Hoshino, M. 2005, JGRA, 110, A02105
Sironi, L., & Spitkovsky, A. 2009, ApJ, 698, 1523
Spitkovsky, A. 2005, in AIP Conf. Proc. 801, Astrophysical Sources of High Energy Particles and Radiation, ed. T. Bulik, B. Rudak, & G. Madejski (Melville, NY: AIP), 345
Umeda, T., Kidani, Y., Matsukiyo, S., & Yamazaki, R. 2012a, PhPl, 19, 042109
Umeda, T., Kidani, Y., Matsukiyo, S., & Yamazaki, R. 2012b, JGRA, 117, A03206
Umeda, T., Kidani, Y., Matsukiyo, S., & Yamazaki, R. 2014, PhPl, 21, 022102
Umeda, T., Yamao, M., & Yamazaki, R. 2011, P&SS, 59, 449
Wilson, L. B., III, Cattell, C. A., Kellogg, P. J., et al. 2009, JGRA, 114, A10106
Wilson, L. B., III, Koval, A., Szabo, A., et al. 2012, GeoRL, 39, L08109
Wilson, L. B., III, Sibeck, D. G., Breneman, A. W., et al. 2014a, JGRA, 119, 6455
Wilson, L. B., III, Sibeck, D. G., Breneman, A. W., et al. 2014b, JGRA, 119, 6475
Wu, C. S., Winske, D., Zhou, Y. M., et al. 1984, SSRv, 37, 63
Yamaguchi, H., Eriksen, K. A., Badenes, C., et al. 2014, ApJ, 780, 136